ORIGINAL ARTICLE

Manufacturing of micro components on amorphous alloy with a high-aspect-ratio characteristic structure by multistage forming method

Sirui Cheng[1,2] · Jiang Ma[1] · Feng Gong[1] · Debin Shan[3] · Chunju Wang[4] · Dongfeng Diao[1] · Jun Shen[1]

Abstract

Amorphous alloys are considered as an ideal material for complex micro component fabrication due to their extraordinary mechanical properties and thermoplastic formability. However, the conventional theories and thermoplastic forming (TPF) methods for amorphous alloys require a lower loading rate and a higher pressure which extremely prolong the processing time and reduce the mold life. In this study, an efficient and low-cost TPF-based method is developed to fabricate the micro impeller by controlling flow states of amorphous supercooled liquid at different forming stages. Based on the finite element simulation results of the filling process and strain distribution, the new multistage forming method enables thin-walled blade fabrication without a significant "dead zone" by adjusting the velocity gradient of the flow front, thus reducing the pressure requirement. Also, the non-Newtonian flow region is proved to be an appropriate TPF window at high temperatures. To verify the validity of the multistage forming method, technological experiments undergoing different conditions were performed. Finally, the full-filled thin-walled blades with a width of 508 μm and surface roughness of 0.25 μm were prepared in about 50 s. This research demonstrates a new TPF-based method for the rapid fabrication of micro components with a high-aspect-ratio characteristic structure in an economic way.

Keywords Amorphous alloy · Multistage forming method · Thin-walled blade · Filling process · Numerical simulation

1 Introduction

Amorphous alloys possess unique physical properties and mechanical properties, such as superior specific strength [1], high hardness [2], large elastic limit [3], excellent corrosion resistance [4], and high wear resistance [5], thereby considering as a category of promising structural and functional materials. Besides, they also attract large interest in the manufacturing field due to the outstanding fluidity in the supercooled liquid

✉ Jun Shen
   junshen@szu.edu.cn

1 College of Mechatronics and Control Engineering, Shenzhen University, Shenzhen 518060, Guangdong, China

2 College of Physics and Optoelectronic Engineering, Shenzhen University, Shenzhen 518060, China

3 School of Materials Science and Engineering, Harbin Institute of Technology, Harbin 150006, China

4 School of Mechanical and Electrical Engineering, Robotics and Microsystems Center, Soochow University, Suzhou 215131, China

(SCLR). Benefiting from this advantage, amorphous alloys are suitable for precisely reproducing the complicated characteristic structures on scales ranging from nanometer to millimeter by thermoplastic forming (TPF) method because they intrinsically overcome the grain size limitations [6–8].

At present, many studies on the TPF-based methods of amorphous micro components have been performed for expanding their application scopes [9]. For example, Schroers et al. [10] formed an amorphous three-dimensional shell by blow molding to achieve the continuous fabrication of the thin-walled pressure vessel. Liu et al. [11] developed a self-aligned multi-ball hot embossing method for preparing the precision mold of the optics microlens array, which can simplify the manufacturing process of compound eye structure. Hasan et al. [12] proposed a high-throughput forming technique for nanostructure arrays to adjust the wettability, cellular response, reflectance, and catalytic activity of amorphous alloy surface. Among these studies, one of the most important applications is the power component in microelectromechanical systems (MEMS). These micro components with better forming qualities play a critical role in

determining the service performance of MEMS, which are expected to achieve a higher power output and a longer service life [13, 14]. Compared with the laser ablation, WEDM and micromachining [15–17], the closed extrusion method possesses a simple manufacturing process and high material utilization rate, thus widely used to fabricate amorphous micro components with complex structural characteristics [18–20]. During the whole closed extrusion process, the friction is usually considered as flow resistance, which prevents amorphous supercooled liquid from replicating the microcavity details and even causes remarkable filling defects. Tuncer et al. [21] proposed the floating extrusion method in order to reduce the load level by changing the flow state of the workpiece. Some researchers explored the filling processes of the power components via the floating extrusion method through FE simulation and experimental methods, thereby providing a reference for predicting the forming qualities and processing route designs [22–24]. However, these traditional isothermal extrusion methods need to create two primary problems [25]: One is that the extremely higher pressure, which rapidly decreases the mold life and makes the costly mold a disposable material, is required to avoid the remarkable filling defects on the micro components. Another is that the TPF process of amorphous alloys is generally performed at a lower loading rate, leading to a long processing time and energy consumption.

In this study, an efficient and low-cost TPF method was developed to produce amorphous micro impellers with high-aspect-ratio thin-walled blades. Due to the variation of friction direction during the multistage forming process, the flow velocity gradient of amorphous liquid could be automatically adjusted once the forming stage changed, thus obtaining the flat flow front to get rid of the larger "dead zone" on the tips of the thin-walled blades. The forming processes at various experimental conditions have also been investigated through FE simulation to analyze the relationship between the filling states of thin-walled blades and the technological conditions. The morphology of thin-walled blades extracted from the simulation result was compared with experimental data to verify the validity of the numerical analysis in guiding the multistage forming process. Besides, a series of technological experiments were conducted using the multistage forming system. On this basis, the full-filled micro impellers were manufactured via the optimized parameters, indicating that the proposed multistage forming method was an effective and cost-saving technique to prepare micro components with a high-aspect-ratio characteristic structure.

2 Experimental methods

2.1 Material preparation and modeling

The alloy ingots with a nominal composition of $Zr_{41.2}Ti_{13.8}Cu_{12.5}Ni_{10}Be_{22.5}$ (at.%, Vit1) were prepared by

arc melting high purity Zr, Ti, Cu, Ni, Be elements (>99.9 wt. %) under a Ti-gettered high-purity argon atmosphere. These ingots were remelted at least four times to ensure their homogeneity, and then suck-cast into a water-cooled copper mold to produce the cylindrical amorphous rods with 10 mm in diameter and 50 mm in length. The microstructural characteristics of these amorphous rods were confirmed by X-ray diffraction (XRD, Philipus X'Pert) with Cu-Kα radiation, and their thermal properties were tested by differential scanning calorimetry (DSC, Perkin Elmer Pyris DSC 1) at the continuous heating rates of 20 K/min under a flow of high purity argon. The test data shows a diffuse halo on the XRD pattern without any diffraction peaks, indicating a fully amorphous structure of these as-cast Vit1 alloy rods. Their characteristic temperatures, the glass transition temperature (T_g), the onset crystallization temperature (T_x), and the supercooled liquid region ($\Delta T_x = T_x - T_g$), are 630 K, 712 K, and 82 K, as shown in Fig. 1. The larger ΔT_x means better structural stability and a wider temperature range for the TPF process, which satisfies the necessary condition for manufacturing the amorphous micro components.

For analyzing the TPF process of the thin-walled blade by the finite element (FE) simulation, a phenomenological Maxwell-extreme model proposed by Wang et al. [26] has been used to describe the deformation behavior of the Vit 1 amorphous alloy, as expressed in Eq. 1. All the parameters in this material model can be obtained from the isothermal compression test data (as listed in Table 1), suggesting that it is easy to be used in FE simulation and improve the calculation efficiency in engineering applications. In addition to the stress-strain curves in SCLR, the boundary between Newtonian and non-Newtonian flow region, which is regarded as an important factor to determine the TPF process
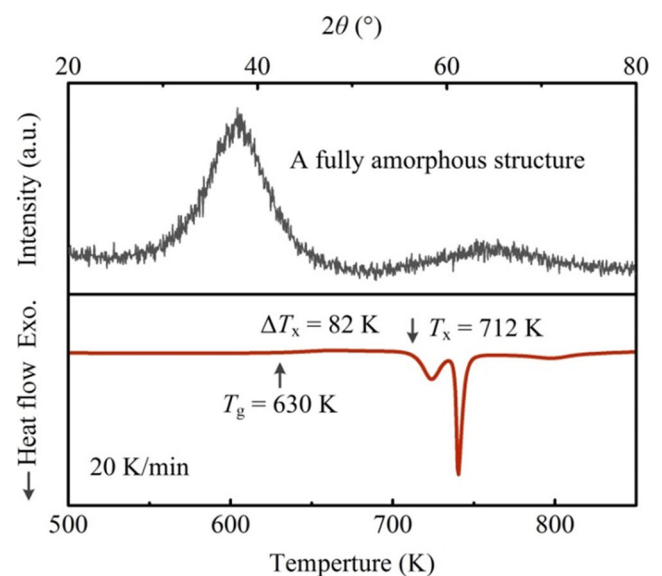
Fig. 1 The XRD pattern (black curve) and DSC result (red curve) of Vit 1 alloy

Table 1 Fitting parameters of the Maxwell-extreme constitutive model for Vit1 alloy

Fitting parameters	Value	Fitting parameters	Value	Fitting parameters	Value
B	1.1×10^{-9}	k	4.4	C_2	-459
H	246 kJ/mol	a	-0.22	C_3	1.6×10^5
t	450	b	160	m	-8.0×10^{-4}
A	4.6×10^{-16}	K	4.4×10^{-5}	n	0.54
H^*	189 kJ/mol	H''	84 kJ/mol	α	-2.6×10^{-5}
w_{avg}	0.04	C_1	0.33	β	1.84

[27], has also been obtained from the Maxwell-extreme model. Figure 2 a shows the normalized viscosity η/η_0 (where η is the apparent viscosity at the steady-state flow stage, and η_0 is the equilibrium viscosity) as a function of the strain rate at different temperatures (633–693 K). It is clear that the bending over appears on the normalized viscosity-strain rate curves, featuring a nonlinear response to true stress and the transition from the Newtonian fluid to the non-Newtonian fluid. Based

on these normalized viscosity data, the processing map has been built to support the need for the experimental parameter design concerning the strain rate and ambient temperatures, as presented in Fig. 2b. In this study, we chose four typical parameters to perform the FE analysis, see the square points in Fig. 2b.

$$\sigma = 3\dot{\varepsilon}B\exp\left(\frac{H}{RT}\right)\left[1-\exp\left(\frac{-1}{tA\exp\left(\frac{H^*}{RT}\right)\dot{\varepsilon}}\right)\right]\left[1-\exp\left(\frac{-\varepsilon}{\lambda_{\mathrm{f}}\dot{\varepsilon}}\right)\right]+\left[K\log\dot{\varepsilon}\exp\left(\frac{H''}{RT}\right)+C(T)\right][\exp(-\exp(-z)-z+1)] \qquad (1)$$

where $\lambda_{\mathrm{f}}=\frac{\sigma_{\mathrm{f}}}{3E\left(T\varepsilon\right)\varepsilon}$, $z=\frac{\varepsilon-\varepsilon_{\mathrm{c}}\left(T\varepsilon\right)}{w_{\mathrm{avg}}}$.

2.2 Multistage forming process design of the micro impeller

Figure 3 shows the 3D geometric object and structural parameters of the micro impeller in our research. It is composed of a cylindrical mandrel with a diameter of 2 mm and six thin-walled blades (here, the length L is 1.5 mm and the thickness T is 0.5 mm). For the conventional closed extrusion method and the floating extrusion method, the higher aspect ratio ($L/T = 3$) is not conducive to viscous flow of amorphous supercooled liquid because of the energy dissipation induced by high interface friction, thus resulting in severe frustration to obtain good structural integrity, particularly at the tips of the thin-walled blades. The multistage forming method aims to replicate the structural details by controlling the flow front of amorphous supercooled liquid at different forming stages. Its entire procedure consists of two stages, as presented in Fig. 4. The early stage of the forming process (stage I) is similar to the closed extrusion method. The amorphous supercooled liquid begins to deform, and the upper portions of the microcavities are preferentially filled because of the axial velocity gradient. The duration of this stage depends on the initial clearance S_1 between the punch and the floating die, see Fig. 4a, b. At stage II, the floating die slides with the punch

until the microcavities are full-filled with the amorphous supercooled liquid. The axial velocity gradient is changed due to the variation of the friction direction, thereby obtaining a flat flow front. For optimizing the filling state of the amorphous supercooled liquid, the duration of stage II can be adjusted by setting different proportions of S_2 in the total punch displacement S_{total} ($S_{\mathrm{total}} = S_1 + S_2$), as shown in Fig. 4c.

2.3 Pre-processing of FE simulation

For investigating whether the multistage forming method can control the flow front of amorphous supercooled liquid and reduce the load requirement of the TPF process, FE simulation is conducted by using the commercially available software Deform 3D. The object subjected to FE analysis is composed of the punch, the bottom die, the floating die, and the cylindrical workpiece with dimensions of $\Phi2 \times 4.11$ mm. The isotropic amorphous supercooled liquid is meshed using 75000 four-node quadrilateral elements to improve the computational accuracy, as shown in Fig. 5. The mold components are assumed to be rigid bodies, and there is no heat transfer between the mold and the workpiece under isothermal condition. Based on the previous works by Lowhaphandu et al. and Bruck et al. [28, 29], the von Mises criterion is used to describe the yield behaviors of amorphous supercooled liquid in our study. The simulation process is divided into two parts
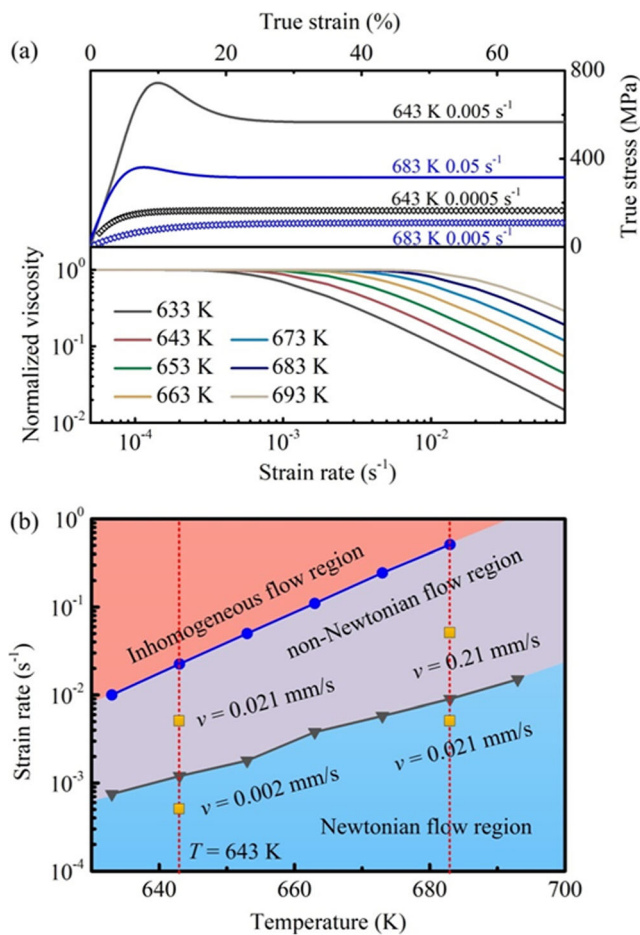
Fig. 2 Flow characteristics of Vit1 alloy in SCLR calculated from the proposed material model. **a** The calculated stress-strain curves and normalized apparent viscosities of Vit1 alloy. **b** The processing map of Vit1 amorphous supercooled liquid including three typical flow modes

corresponding to the closed extrusion stage and the floating extrusion stage. First, the punch moves downward with a constant velocity to impose an axial load on the workpiece. When the punch displacement exceeds the set value S_1, the floating die will follow the punch with the same velocity until the end
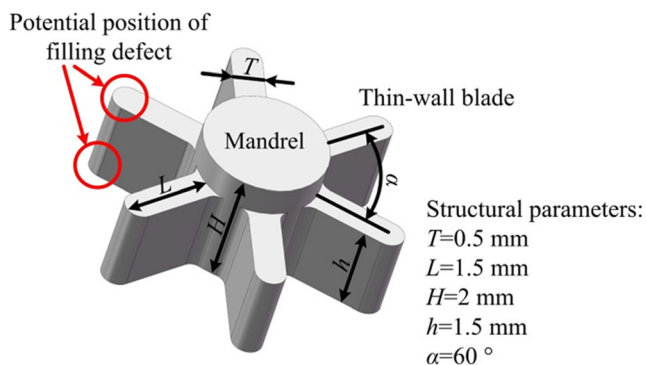
Fig. 3 Structural parameters of the micro impeller with six thin-walled blades

of the TPF process (here the total punch displacement S_{total} = 2.11 mm).
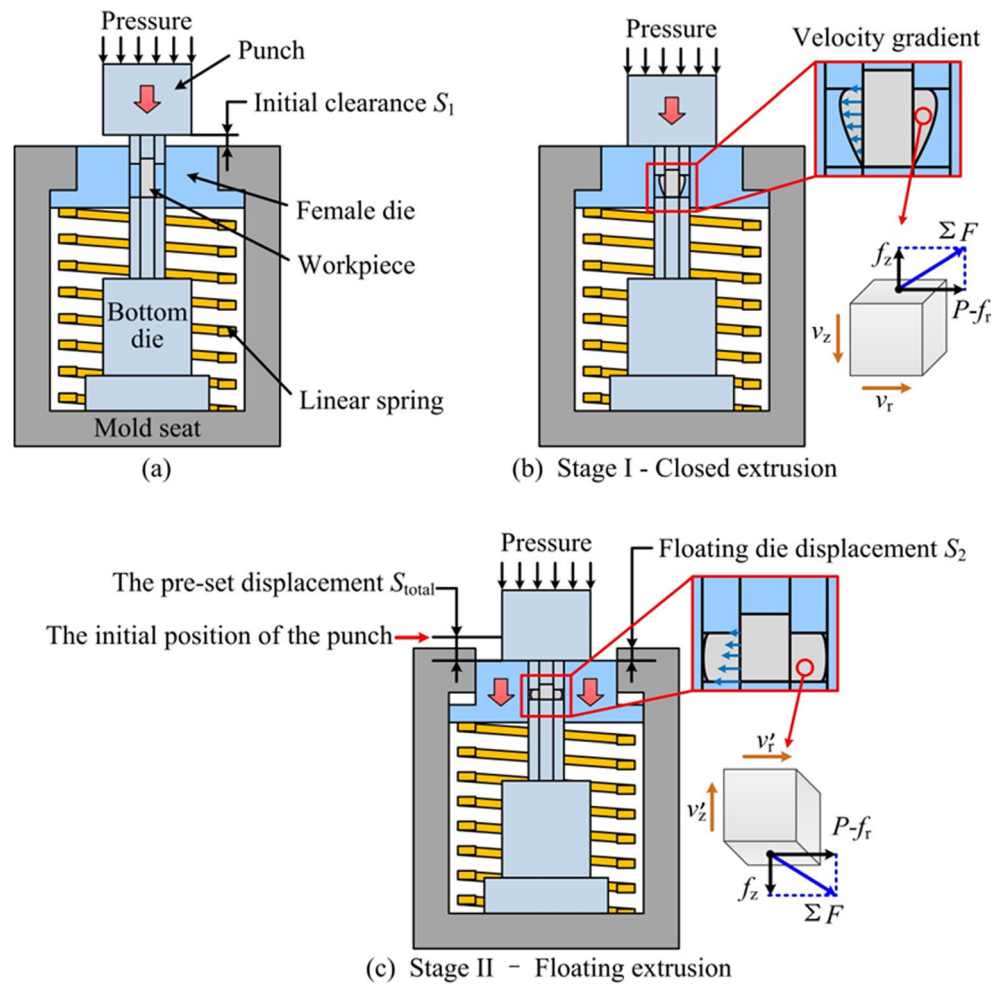
2.4 Multistage forming system

Technical experiments of the thin-walled blades have been carried out to verify the forming process obtained from FE simulation. The built manufacturing platform consists of four parts: a programmable control system to set the loading path, an independent temperature monitoring system to accurately adjust the temperature of the heating equipment and reflect the temperature near the workpieces, a universal loading system (electronic universal testing machine), and a multistage forming device (including a mold seat, a punch, a bottom die, and a floating die), as depicted in Fig. 6a. The machining accuracy of the mold components directly determines the forming qualities of the thin-walled blades, so the core components of the extrusion die are fabricated using a low-speed wire electrical discharge machining (LS-WEDM) to ensure their geometric dimension and surface roughness, as shown in Fig. 6b–d. The measurement results from laser scanning confocal microscopy (LSCM) indicate that the microcavity width of the thin-walled blade is 524 μm, and the surface roughness of the punch and bottom die is Ra 0.12 μm, which can satisfy the requirements of micro impeller fabrication, as presented in Figs. 6e, f.

3 Numerical simulation of the multistage forming process

3.1 Filling process of the amorphous supercooled liquid

By extracting the simulation data, the structural characteristic, velocity gradient, and strain distributions of the amorphous supercooled liquid can be investigated and used as the reference for designing the TPF route of the thin-walled blades. Figure 7a shows the flow velocity-time curves of three different points on the workpiece (temperature is 683 K, loading rate is 0.041 mm/s, and the flow behavior of amorphous supercooled liquid yields to the non-Newtonian flow mode). At the early stage (stage I), the flow velocity of points 1 and 2 increases gradually as the punch displacement increases. However, the flow velocity of point 3 is maintained at a lower level (less than 0.01 mm/s) owing to the surface friction between the workpiece and the bottom die. When the TPF process enters stage II (processing time t = 36.46 s), the flow velocity of point 1 reduces to 0.0014 mm/s in about 0.25 s, meanwhile, the flow velocity of point 3 dramatically increases to about 0.047 mm/s. The flow velocity fields before and after the stage transition have been presented in Figs. 7b, c. The variation of the flow velocity gradient, which matches well

Fig. 4 Schematic of the multistage forming method for fabricating micro impellers. **a** Primary structure of multistage forming devices. **b** The early stage corresponding to the closed extrusion process. **c** The final stage corresponding to the floating extrusion process


(a)

(b) Stage I - Closed extrusion

(c) Stage II – Floating extrusion

with the expected result in the processing design, causes a flat flow front at the end of the forming process (step 420), as seen in Fig. 7d. Additionally, the full-filled thin-walled blades are formed by the multistage forming method with a compressing load of 7.79 kN, which is significantly lower than those produced by the closed extrusion and floating extrusion methods, as shown in Fig. 8. This is mainly because the flat flow front avoids the insufficient filling at the tips of the thin-walled blades and makes it unnecessary to drive the amorphous

supercooled liquid to fill these residual "dead zone." These FE simulation results indicate that the expected objectives for optimizing the flow front and reducing the load requirement are basically satisfied.

3.2 Effects of the flow mode on the strain distribution

According to previous studies [30], the metastable structure of amorphous alloy can be changed during hot deformation, thus

Fig. 5 FE simulation object of the multistage forming method for micro impeller: assembly method of the main components for the multistage forming device and partially enlarged view of the meshed workpiece and mold components, as well as their contact forms.
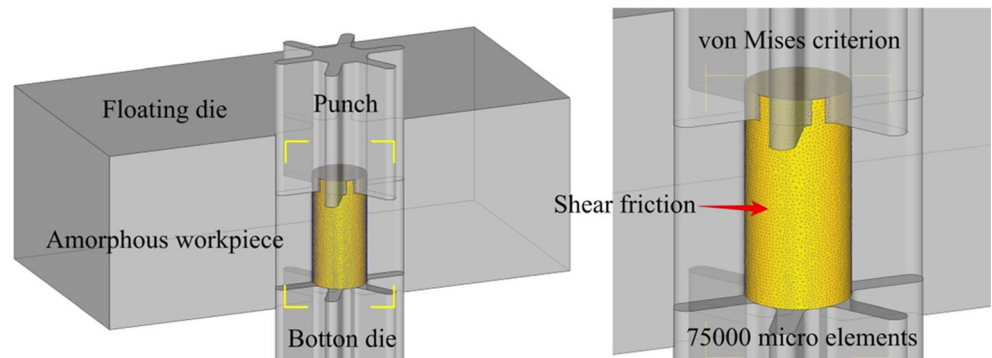
Fig. 6 Manufacturing platform of amorphous micro impellers. **a** Manufacturing system that comprises a pressure control system, a temperature monitoring system, a loading system, and the structural detail of the multistage forming apparatus for micro impellers. **b**–**f** The morphological characteristics, dimensional accuracy, and surface quality of the core components of the micro mold (punch, bottom die, and floating die)
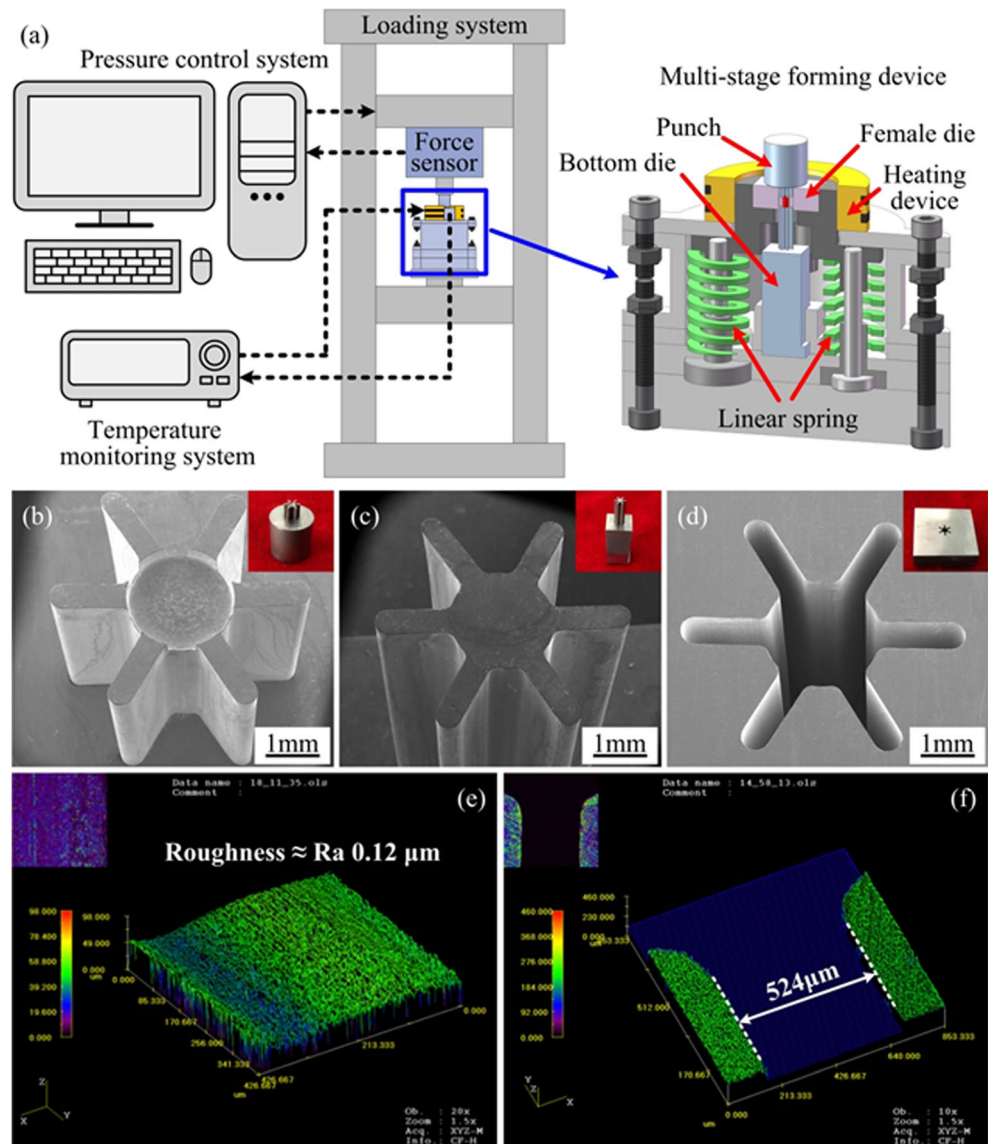
affecting the mechanical properties of the prepared components. However, the microstructure evolution induced by plastic strain is difficult to verify by direct observation, so the FE simulation results of strain distribution are extracted to indirectly predict the microstructure state in the Newtonian and non-Newtonian workpiece. Also, the profile shapes of thin-walled blades under different processing conditions are investigated. Figure 9a shows the effective strain distribution of the Newtonian fluid workpiece ($T = 643$ K, $v = 0.002$ mm/s) at the end of the TPF process. We noticed that a conspicuous high strain region forms at the lower portion of the thin-walled blade, meanwhile, the insufficient filling is retained in the middle of the thin-walled blade and becomes the potential position for defect formation. To semi-quantitatively evaluate the strain state in the workpiece, the simulation data of the effective strain in each

microelement are extracted. The number of Newtonian and non-Newtonian microelements with various effective strain levels are plotted in Fig. 9c. In general, a large number of deformed microelements will be concentrated in a single range if the effective strain is uniformly distributed in the workpiece. Conversely, a plurality of statistical peaks can be observed in different effective strain ranges, indicating the significant strain difference among the deformed microelements. The proportion of the Newtonian fluid microelements with a lower effective strain (0–0.7 mm/mm) is about 70%, and only 2% of the microelements have "high" effective strain (more than 2.1 mm/mm), see the gray bar in Fig. 9c. For those non-Newtonian fluid workpieces ($T = 643$ K, $v = 0.021$ mm/s), the high strain region is mainly distributed at the upper portion of the thin-walled blade (see Fig. 9b), and the effective strain in about 30% microelements exceeds 2.1 mm/mm, as
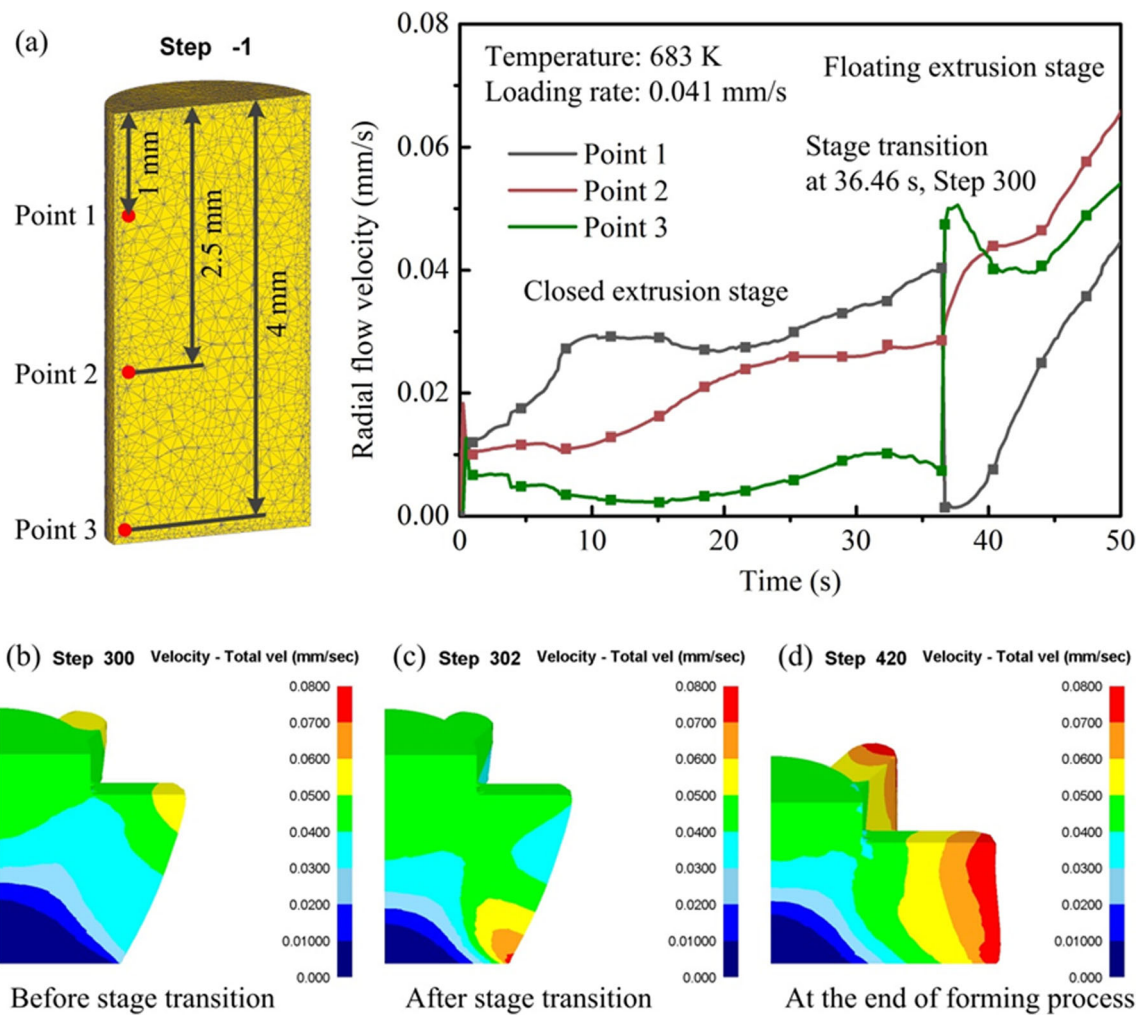
Fig. 7 Filling states of the amorphous supercooled liquid at $T = 683$ K, $v = 0.041$ mm/s. **a** Flow velocity curves of the three different points; the flow velocity fields of the thin-walled blades at **b** 36.46 s, **c** 36.7 s, and **d** 51.06 s
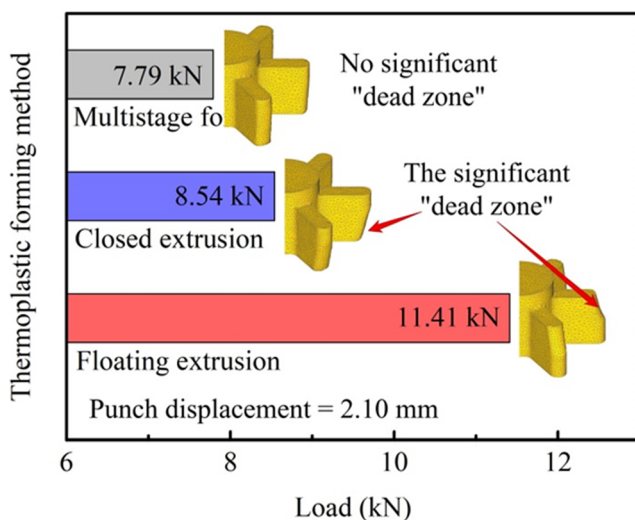

Fig. 8 The load requirement for the different TPF-based methods. The "dead zone" at the tips of the thin-walled blades should be considered as the main reason for the higher load requirements

marked by the blue bar in Fig. 9c. It is deduced that Newtonian flow mode can guarantee the uniform effective strain distribution in workpiece due to better fluidity and simple flow behaviors, but lower viscous resistance makes the friction conditions affect the flow behaviors of the Newtonian fluid workpiece more easily, leading to a potential filling defect on the thin-walled blade.

As the experimental temperature increases to 683 K, the Newtonian fluid ($v = 0.021$ mm/s) and the non-Newtonian fluid workpieces ($v = 0.21$ mm/s) display a similar strain distribution state, and the statistical data also indicates that no notable proportional difference in effective strain can be found between the two amorphous fluid workpieces, see Fig. 10a–c. These simulation results can be attributed to larger amounts of activation volume induced by higher temperature, causing that the microstructural response of the non-Newtonian fluid workpiece is fast enough to support the need for atomic rearrangement. Besides, there are no significant insufficient fillings on these two kinds of amorphous supercooled liquid. Based on these

Fig. 9 Strain distribution states in Newtonian and non-Newtonian fluid workpieces. **a** 643 K, Newtonian fluid, step 420. **b** 643 K, non-Newtonian fluid, step 420. **c** Their statistical results
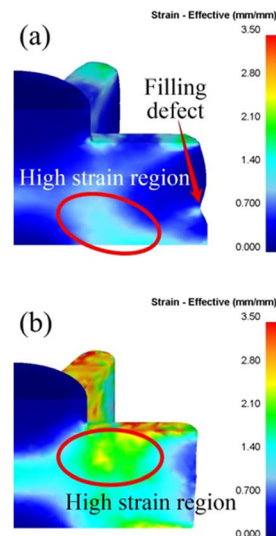
simulation results, it can be clearly concluded that when the temperature approaches T_x, the flow mode is no longer the main factor determining the filling process and strain state of the workpiece. So the TPF windows of amorphous alloys are extended to the non-Newtonian flow region, and the higher loading rate can be chosen as the processing parameter.

4 Experimental results and discussion

4.1 Technological experiment of the multistage forming method

4.1.1 TPF process verification

A comparison of structural characteristics for those micro impellers formed by the three different methods is depicted in
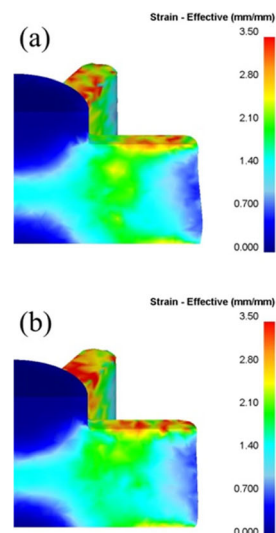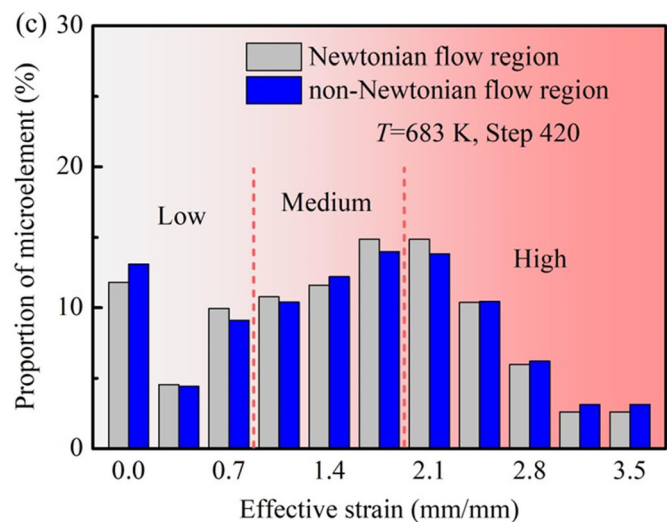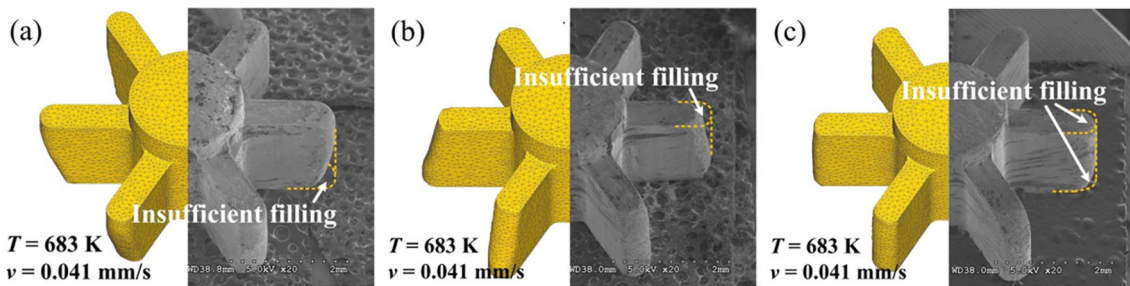
Fig. 11. The obvious insufficient fillings are located at the lower tips of the thin-walled blades undergoing closed extrusion. In contrast, the floating extrusion process makes the larger insufficient fillings retain at the upper tips of the thin-walled blades. These experimental results are basically consistent with the simulation results. Compared with the two situations above, there are only smaller defects on the tips of the multistage-formed blades, indicating better adaptability of the multistage forming method in the thin-walled structure with a high-aspect-ratio. Take the forming process of the thin-walled blade with an experimental temperature of 683 K and a loading rate of 0.041 mm/s as an example; the filling states of the workpieces at different TPF stages (the punch displacement is 0.8 mm, 1.5 mm, 2.0 mm, 2.11 mm) are presented in Fig. 12. The non-Newtonian amorphous supercooled liquid preferentially fills into the upper portion of the microcavities during the initial stage (punch

Fig. 10 Strain distribution states in Newtonian and non-Newtonian fluid workpieces. **a** 683 K, Newtonian fluid, step 420. **b** 683 K, non-Newtonian fluid, step 420. **c** Their statistical results

Fig. 11 The insufficient fillings on the thin-walled blades undergoing three different forming methods. **a** Closed extrusion. **b** Floating extrusion. **c** Multistage forming method

displacement is about 0.8 mm), as shown in Fig. 12a. As the punch displacement increases to 1.5 mm, the TPF process of the thin-walled blades enters the floating extrusion stage. The amorphous supercooled liquid begins to fill the bottom of the microcavities, as illustrated in Fig. 12b. It can be seen that there is an obvious zig-zag flow front within the middle of each thin-walled blade. These phenomena via technological experiments demonstrate good agreement with FE simulation results. When the punch displacement approaches 2.0 mm, the insufficient filling induced by the zig-zag flow front can still be observed on some thin-walled blades, but becomes smaller during the TPF process, as depicted in Fig. 12c. Ideally, the whole forming stage of the thin-walled blades should be complete when the punch displacement reaches 2.11 mm. However, Fig. 12d displays that the structural details of the microcavities are not full-filled because of the elastic

deformation of the manufacturing platform (including the loading device and mold components), causing that the plastic deformation of the workpiece does not reach the theoretical value. As such, the total displacement needs to be corrected by considering the elastic deformation of the loading system and the workpiece to obtain the thin-walled blades with integrated structural details.

4.1.2 TPF process optimization

The primary challenge to fabricate the thin-walled blade is to maintain the good fluidity of amorphous supercooled liquid during the whole forming process. Based on the study by Bochtler et al. [31], the determinants of thermoplastic formability improvement are the temperature condition and strain rate, which directly determine the viscous resistance of

Fig. 12 Filling states of amorphous supercooled liquid at different stages of the TPF process. Punch displacement is **a** 0.8 mm, **b** 1.5 mm, **c** 2.0 mm, and **d** 2.11 mm
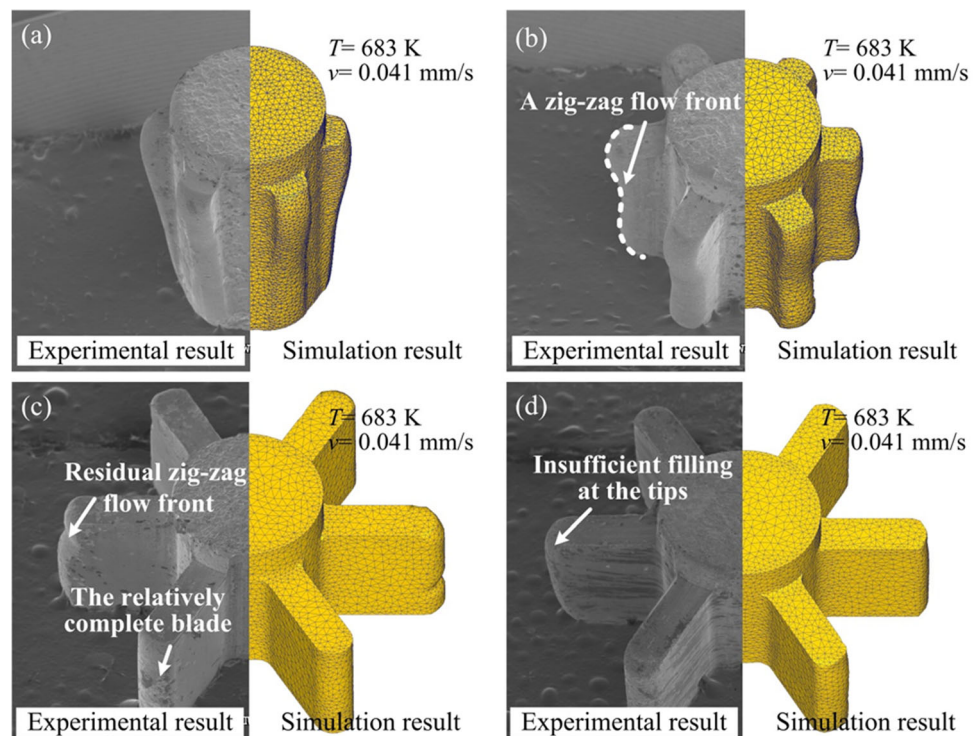
amorphous supercooled liquid. Therefore, the TPF route of thin-walled blades will be optimized by adjusting the ambient temperature and loading rate. Figure 13 shows the structural characteristics of the thin-walled blades undergoing different loading rates. It is clear from the figure that the thin-walled blades have lower filling rates within the lower loading rate range of 0.004–0.021 mm/s, which are usually considered as favorable conditions for obtaining better formability, as seen in Fig. 13a–c. Conversely, Fig. 13d shows that the fully formed micro impeller can be obtained when the loading rate reaches 0.041 mm/s. It reveals that the low loading rate is unfavorable to the TPF process of the thin-walled blade, which is contrary to the theoretical prediction. The possible reason may be that despite the TPF window in SCLR, the microstructural evolution from the amorphous phase to the crystalline phase may be completed in less than 5 min at a temperature close to T_x [32–34]. The low loading rate can easily make the duration of the TPF process exceed the crystallization time, causing a significant thermoplastic formability drop. In order to guarantee the better thermoplastic formability of the amorphous supercooled liquid, a relatively high loading rate range should be selected to reduce the processing time and provide the best compromise between thermoplastic formability and the crystallization process, meanwhile, the high processing efficiency of amorphous micro impellers is also the most immediate benefit of the higher loading rate.

Figure 14 illustrates the overviews (SEM images) of the amorphous micro impellers at different temperatures (the loading rate is 0.041 mm/s). With the increase of temperature,

the amorphous supercooled liquid transforms from non-Newtonian fluid to Newtonian fluid. However, the micro impellers formed at different temperatures possess similar structural characteristics. These results agree well with the simulation results and further confirm that the effects of flow mode on the TPF process can be ignored under the higher temperature level. It is worth noting that the residual filling defects can be discovered in the middle of the thin-walled blades (see Fig. 14d), revealing that the thermoplastic formability of the amorphous supercooled liquid cannot be enhanced by simply increasing the ambient temperature. Although this result is inconsistent with the previous conclusion [35], it does not challenge the found correlation. As well known, even if the TPF temperature is lower than T_x, the metastable structure still prone to forming the ordered clusters [36, 37], leading to a thermoplastic formability drop of the amorphous supercooled liquid and an unsatisfied filling process. Hence, the TPF temperature should be set within an appropriate range to keep the better fluidity of the amorphous supercooled liquid.

4.2 Forming qualities of the micro impeller

The amorphous micro impellers subjected to the optimized processing parameters (forming temperature, 683 K; loading rate, 0.041 mm/s) are depicted in Fig. 15a, b. In this case, the amorphous micro impeller with good structural integrity is formed in around 50 s, and no visible filling defects are discovered on the thin-walled blades. LSCM results reveal that

Fig. 13 SEM photographs of the formed micro impellers under different loading rates. a 0.004 mm/s. b 0.008 mm/s. c 0.021 mm/s. d 0.041 mm/s
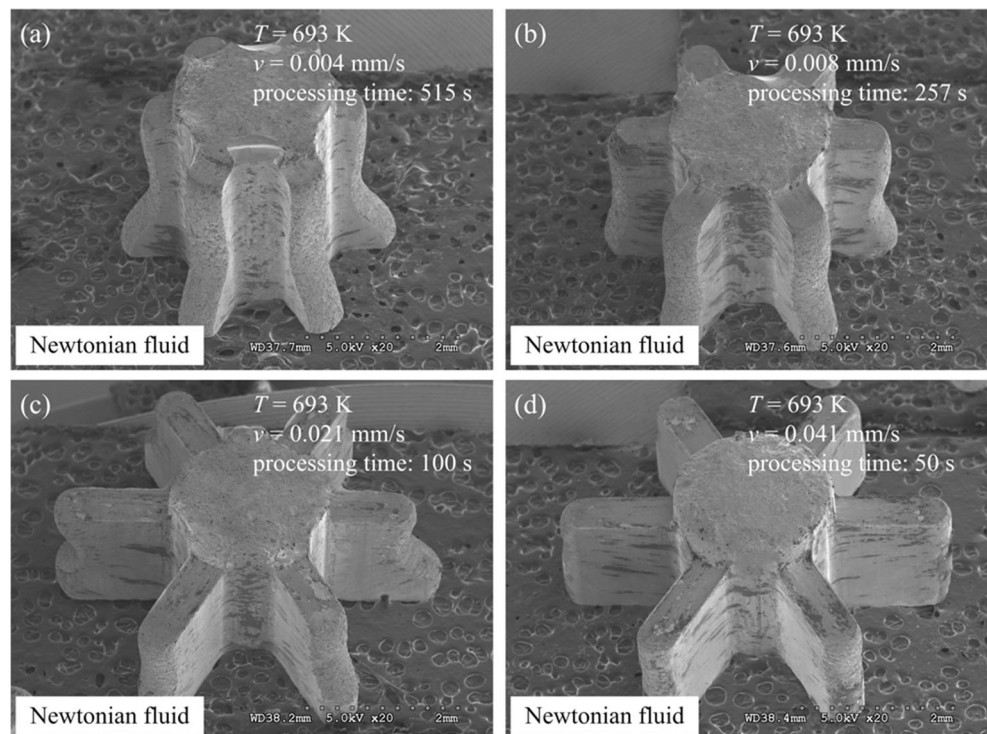
Fig. 14 SEM images of the filling results of micro impellers at different temperatures. **a** $T = 663$ K. **b** $T = 673$ K. **c** $T = 683$ K. **d** $T = 693$ K
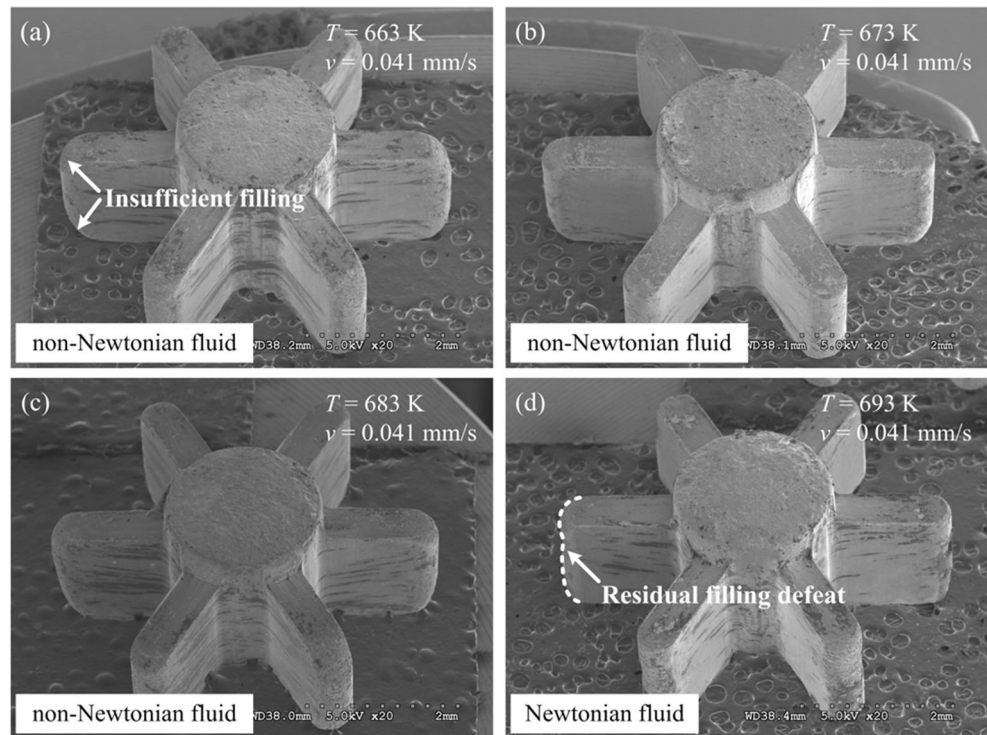
all the thin-walled blades possess a higher dimensional accuracy with a mean width of 508 μm, which is slightly smaller than that of the die cavity (mean width of 524 μm), as shown in Figs. 15c. The annihilation of the free volume induced by plastic deformation and the cooling shrinkage after the TPF process are the main reasons for the variation of the geometric dimension. Figure 15d shows that the surface roughness of the prepared thin-walled blades is about Ra 0.25 μm, which is higher than that of the machined cavity surface of the floating die (Ra 0.12 μm). Meanwhile, a few scratches with a width of

Fig. 15 **a** The formed amorphous micro impeller under an optimized processing condition. **b** SEM image of the amorphous micro impeller. **c**, **d** Forming qualities of the amorphous micro impeller, including the width of the thin-walled blades and the surface roughness measured by LSCM
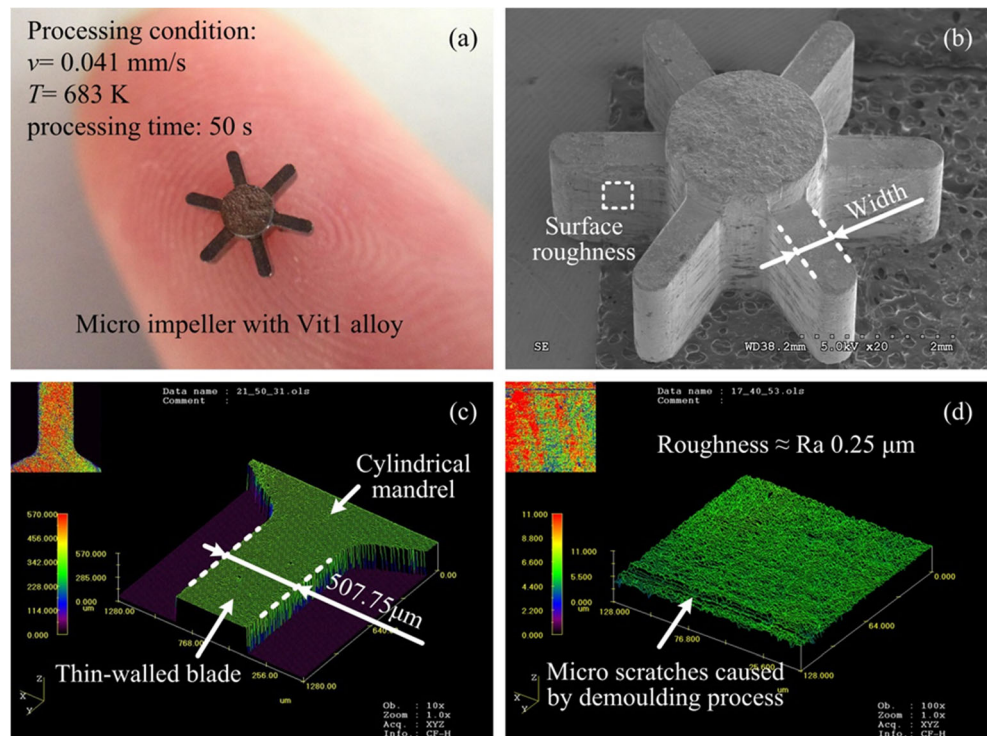
5–8 μm can be observed on the thin-walled blades. These surface defects are created by the sliding between the microcavity and the workpiece during the demolding process. It means that the friction condition not only has a distinct influence on the flow state of the amorphous supercooled liquid but also determines the surface qualities of thin-walled blades. According to these test results, we conclude that thin-walled blades with a higher aspect ratio and better forming accuracy can be prepared via the novel processing sequence.

5 Conclusions

This paper demonstrates a high efficient and low-cost TPF-based method for the amorphous micro impellers by combining the closed extrusion and floating extrusion process. The main conclusions are summarized as follows:

(1) The multistage forming method can adjust the flow front by changing the flow velocity gradient in different forming stages, which avoids the "dead zone" at the tips of the thin-walled blade so as to reduce the load requirement of the TPF process.

(2) Similar profile shapes and strain distribution of Newtonian fluid and non-Newtonian fluid workpieces are observed at the temperature of 683 K. It reveals that the non-Newtonian fluid workpiece can be used in TPF of the amorphous alloy at a temperature close to T_x.

(3) The microstructure evolution during the TPF process plays an important role to determine the fluidity of amorphous supercooled liquid. The better thermoplastic formability cannot be obtained by simply increasing the ambient temperature or decreasing the loading rate. The thermoplastic formability drop induced by high temperature and long processing time should be considered while selecting the TPF window.

(4) The micro impellers with good structural integrity have been successfully prepared by the optimized multistage forming method in about 50 s. These formed thin-walled blades with non-Newtonian amorphous workpiece possess higher dimensional accuracy (mean width 508 μm) and lower surface roughness (Ra 0.25μm).

(5) This new TPF method provides great potential for the MEMS field such as microgenerators and micropumps and offers a useful alternative to the fabrication of micro components with high-aspect-ratio thin-walled structures.

Declarations

References

1. Sun F, Wang B, Luo F, Yan YQ, Ke HB, Ma J, Shen J, Wang WH (2020) Shear punching of bulk metallic glasses under low stress. Mater Design 190:108595

2. Li B, Sun WC, Qi HN, Lv JW, Wang FL, Ma MZ, Zhang XY (2020) Effects of Ag substitution for Fe on glass-forming ability, crystallization kinetics, and mechanical properties of Ni-free Zr-Cu-Al-Fe bulk metallic glasses. J Alloys Compd 827:1–10

3. Wu WZ, Jiang JL, Li GW, Fuh JYH, Jiang H, Guo PW, Zhang LJ, Li W, Zhao J (2019) Ultrasonic additive manufacturing of bulk Ni-based metallic glass. J Non-Cryst Solids 506:1–5

4. Khan MM, Shabib I, Haider W (2019) A combinatorially developed Zr-Ti-Fe-Al metallic glass with outstanding corrosion resistance for implantable medical devices. Scr Mater 162:223–229

5. Li X, Liang X, Ma J, Shen J (2020) Cold joining to fabricate large size metallic glasses by the ultrasonic vibrations. Scr Mater 185:100–104

6. Kumar G, Tang HX, Schroers J (2009) Nanomoulding with amorphous metals. Nature 457(7231):868–872

7. Ma J, Huo LS, Zhao DQ, Wang WH (2013) Micro mold filling kinetics of metallic glasses in supercooled liquid state. J Appl Phys 113:104505

8. Inoue A, Takeuchi A (2011) Recent development and application products of bulk glassy alloys. Acta Mater 59:2243–2267

9. Qin Y, Brockett A, Ma Y, Razali A, Zhao J, Harrison C, Pan W, Dai X, Loziak D (2010) Micro-manufacturing: research, technology outcomes and development issues. Int J Adv Manuf Technol 47:821–837

10. Schroers J, Pham Q, Peker A, Paton N, Curtis RV (2007) Blow molding of bulk metallic glass. Scr Mater 57:341–344

11. Liu XH, Mo RD, Li KS, Shen J, Ma J, Gong F (2020) Manufacturing of 3D microlens array mold on bulk metallic glass by self-aligned multi-ball hot embossing. Int J Pr Eng Man-GT 8:1209–1223. https://doi.org/10.1007/s40684-020-00266-8

12. Hasan M, Kumar G (2017) High-throughput drawing and testing of metallic glass nanostructures. Nanoscale 9:3261–3268

13. Skrzypacz J, Bieganowski M (2018) The influence of micro grooves on the parameters of the centrifugal pump impeller. Int J Mech Sci 144:827–835

14. Tan L, Zhu BS, Cao SL, Bing H, Wang YM (2014) Influence of blade wrap angle on centrifugal pump performance by numerical and experimental study. Chin J Mech Eng-En 27:171–177

15. Kim B, Nam HK, Watanabe S, Park S, Kim Y, Kim YJ, Fushinobu K, Kim SW (2020) Selective laser ablation of metal thin films using ultrashort pulses. Int J Pr Eng Man-GT 8:771–782. https://doi.org/10.1007/s40684-020-00272-w

16. Zhang YM, Zhang Z, Zhang GJ, Li WY (2020) Reduction of energy consumption and thermal deformation in WEDM by magnetic field assisted technology. Int J Pr Eng Man-GT 7:391–404

17. Yi J, Wang XB, Jiao L, MX L, Xiang JF, Yan P, Wang Z (2017) Study in dimension precision of micro straight thin wall with Ti-6Al-4V titanium alloy under mesoscale. Int J Adv Manuf Technol 91:4371–4381

18. Luo SY, Yao JN, Jia L, Du H, Liu HY, Yu FP (2020) Influence of forging velocity on temperature and phases of forged Ti-6Al-4V turbine blade. J Mater Res Technol 9:12043–12051

19. Liu LB, Sun JF, Chen WJ, Zhang J (2017) Finite element analysis of machining processes of turbine disk of Inconel 718 high-temperature wrought alloy based on the theorem of minimum potential energy. Int J Adv Manuf Technol 88:3357–3369

20. Ma YJ, Cheng G (2017) Forming property and broaching error prediction of a forged nickel-based superalloy turbine disc. Aerosp Sci Technol 62:55–64

21. Tuncer C, Dean TA (1987) Die design alternatives for precision forging hollowing parts. Int J Mach Tools Manuf 27:65–76

22. Ryu CH, Joun MS (2001) Finite element simulation of the cold forging process having a floating die. J Mater Process Technol 112:121–126

23. Song MC, Lee YU, VanTyne CJ, Moon YH (2016) Symmetric bending technology using a floating die to forge crank throws for marine engines. J Mater Process Technol 237:197–207

24. Yang C, Zhao SD (2011) Effect of floating die on tooth filling of spur gear forging. Adv Mater Res 295–297:1631–1634

25. Cai J, Dean TA, Hu ZM (2004) Alternative die designs in net-shape forging of gears. J Mater Process Technol 150:48–55

26. Wang CJ, Cheng SR, Ma MZ, Shan DB, Guo B (2016) A Maxwell-extreme constitutive model of Zr-based bulk metallic glass in supercooled liquid region. Mater Design 103:75–83

27. Li N, Chen Y, Jiang MQ, Li DJ, He JJ, Wu Y, Liu L (2013) A thermoplastic forming map of a Zr-based bulk metallic glass. Acta Mater 61:1921–1931

28. Lowhaphandu P, Ludrosky LA, Montgomery SL, Lewandowski JJ (2020) Deformation and fracture toughness of a bulk amorphous Zr-Ti-Ni-Cu-Be alloy. Intermetallics 8:487–492

29. Bruck HA, Christman T, Rosakis AJ, Johnson WL (1994) Quasi-static constitutive behavior of $Zr_{41.25}Ti_{13.75}Ni_{10}Cu_{12.5}Be_{22.5}$ bulk amorphous alloys. Scr Met Mater 30:429–434

30. Cheng SR, Wang CJ, Ma MZ, Shan DB, Guo B (2016) Mechanism for microstructural evolution induced by high temperature deformation in Zr-based bulk metallic glasses. J Alloys Compd 676:299–304

31. Bochtler B, Kruse O, Busch R (2020) Thermoplastic forming of amorphous metals. J Phys-Condens Ma 32:244002

32. Schroers J (2008) On the formability of bulk metallic glass in its supercooled liquid state. Acta Mater 56:471–478

33. Hua NB, Zhang T (2014) Glass-forming ability, crystallization kinetics, mechanical property, and corrosion behavior of Zr-Al-Ni-Ag glassy alloys. J Alloys Compd 602:339–345

34. Waniuk T, Schroers J, Johnson WL (2003) Timescales of crystallization and viscous flow of the bulk glass-forming Zr-Ti-Ni-Cu-Be alloys. Phys Rev B 67:184203

35. Pitt EB, Kumar G, Schroers J (2011) Temperature dependence of the thermoplastic formability in bulk metallic glasses. J Appl Phys 110:043518

36. Ma J, Zhang XY, Wang DP, Zhao DQ, Ding DW, Liu K, Wang WH (2014) Superhydrophobic metallic glass surface with superior mechanical stability and corrosion resistance. Appl Phys Lett 104:173701

37. Jiang HR, Bochtler B, Frey M, Liu Q, Wei XS, Min Y, Riegler SS, Liang DD, Busch R, Shen J (2020) Equilibrium viscosity and structural change in the $Cu_{47.5}Zr_{45.1}Al_{7.4}$ bulk glass-forming liquid. Acta Mater 184:69–78